



Simplify your imaging workflows

**Make research imaging workflows accessible, traceable,
and secure with Athena Software for Core Imaging Facilities.**

Thermo Scientific™ Athena Software is a premium imaging data management platform designed for core imaging facilities that support materials science research.

Athena Software ensures traceability of images, metadata, and experimental workflows through an intuitive and collaborative web interface.

Find out more at thermofisher.com/athena

ThermoFisher
SCIENTIFIC

All-Nanofiber Self-Powered Skin-Interfaced Real-Time Respiratory Monitoring System for Obstructive Sleep Apnea-Hypopnea Syndrome Diagnosing

Xiao Peng, Kai Dong, Chuan Ning, Renwei Cheng, Jia Yi, Yihan Zhang, Feifan Sheng, Zhiyi Wu,* and Zhong Lin Wang*

Human respiration is an indispensable physiological behavior of the body, which is an important indicator to evaluate health status, especially for sleep-related diseases. A real-time respiratory monitoring and sleep breathing detecting system with convenience, high sensitivity, simple fabrication, and wearing comfort still remains a challenge and urgently desirable. Here, a breathable, highly sensitive, and self-powered electronic skin (e-skin) based on a triboelectric nanogenerator (TENG) is reported for real-time respiratory monitoring and obstructive sleep apnea-hypopnea syndrome (OSAHS) diagnosis. By using multilayer polyacrylonitrile and “polyamide 66” nanofibers as the contact pairs, and deposited gold as the electrodes, a contact-separation type of TENG-based all-nanofiber e-skin is developed. The e-skin has a peak power density of 330 mW m^{-2} , high pressure sensitivity of 0.217 kPa^{-1} , excellent working stability, and good air permeability. Therefore, the e-skin is simultaneously capable of energy autonomy and accurate real-time subtle respiration monitoring. Meanwhile, a self-powered diagnostic system for real-time detection and severity evaluation of obstructive sleep apnea-hypopnea syndrome are further developed to prevent the occurrence of OSAHS, delay its development, and improve sleep quality. This study hopes to pave a new and practical pathway for real-time respiration monitoring and sleep breathing diseases clinical detection.

1. Introduction

Wearable electronics have aroused great interests in the field of personal healthcare monitoring. As the indispensable spontaneous behavior of human beings, respiration is not only an essential mechanism to sustain life by ensuring the exchange of oxygen and carbon dioxide but also can be used as crucial feature to assess an individual's health or progression of an disease.^[1] Reasonable monitoring of respiratory states is crucial for forecasting health problems, such as obstructive sleep apnea-hypopnea syndrome (OSAHS), asthma, hyper- or hypoventilation, respiratory alkalosis, pneumonia, lung disease, and so on.^[2] Severe breathing problems can even cause respiratory failure, which is difficult to predict and can be life-threatening within minutes.

Therefore, real-time and continuous monitoring of respiratory activity is very important to identify or predict high-

risk situations and even save lives. At present, the traditional clinical respiration monitoring systems typically include the invasive method of endotracheal intubation nostril and the mild noninvasive method of respiratory mask.^[3–5] However, due to their poor accessibility, cumbersome devices, high cost, uncomfortable use experience, and reliance on external power sources, the widespread adoption of these methods for home/personal healthcare and continuous monitoring is restricted. In recent years, the advances in network technology and low power electronics have achieved great progress of wearable breathing sensors for real-time respiratory monitoring. Many efforts have been devoted to wearable sensors based on the respiratory related signals, including temperature,^[6,7] humidity,^[8–11] airflow^[12–14] as well as the movement of chest and abdomen.^[15–18] On the one hand, humidity, temperature, and airflow sensors used for monitoring respiration have been attached on skin or installed in mask near the nose and mouth, which are susceptible to the environment, uncomfortable and unaesthetic in practical application.^[19,20] On the other hand, strain and pressure sensors usually monitor stress/strain in the chest and abdomen in the form of belts or patches.^[21–23] Compared with the bound feeling of belts, patches have more advantages such as small size,

X. Peng, Prof. K. Dong, C. Ning, R. Cheng, J. Yi, Y. Zhang, F. Sheng, Prof. Z. Wu, Prof. Z. L. Wang
Beijing Institute of Nanoenergy and Nanosystems
Chinese Academy of Sciences
Beijing 100083, P. R. China
E-mail: wuzhiyi@binn.cas.cn; zhong.wang@mse.gatech.edu

X. Peng, Prof. K. Dong, C. Ning, R. Cheng, Y. Zhang, Prof. Z. Wu, Prof. Z. L. Wang
College of Nanoscience and Technology
University of Chinese Academy of Sciences
Beijing 100049, P. R. China

J. Yi, F. Sheng
School of Chemistry and Chemical Engineering
Guangxi University Nanning
Nanning 530004, P. R. China

Prof. Z. Wu, Prof. Z. L. Wang
CUSPEA Institute of Technology
Wenzhou, Zhejiang 325024, P. R. China

Prof. Z. L. Wang
School of Materials Science and Engineering
Georgia Institute of Technology
Atlanta, GA 30332, USA

 The ORCID identification number(s) for the author(s) of this article can be found under <https://doi.org/10.1002/adfm.202103559>.

DOI: 10.1002/adfm.202103559

lightweight, and unobtrusive. However, most patch sensors take the films as electrodes or substrates, which may cause skin discomfort, even inflammation and itching. Therefore, it is desperately desirable to develop a noninvasive, flexible, comfortable, and continuous real-time respiratory monitoring system.

Inspired by the properties of human skin, electronic skins (e-skins) are able to imitate the complicated human sensation. It has a wide range of applications in wearable health monitoring,^[24,25] artificial intelligences,^[26,27] human-machine interfaces,^[28,29] and intelligent robotics.^[30,31] Based on different electromechanical sensing principles, such as capacitance, piezoresistivity, piezoelectricity, and triboelectricity, e-skins are able to detect and quantify the environmental stimuli by transforming them into real-time and visualized electrical impulses.^[32] In particular, triboelectric nanogenerator (TENG) is an emerging technology for energy harvesting, which can convert pervasive mechanical energy into electrical energy based on the coupling effect of triboelectrification and electrostatic induction.^[33] Due to its low cost, simple structure, easy to fabricate, and diverse material option,^[34–42] TENG has broad application potentials in both wearable power supplying and self-powered sensing. In addition, abdominal contraction and dilatation are the natural behaviors in the process of human respiration, which may provide a sustainable biokinetic energy source for TENGs. Therefore, TENG-based e-skin with the merits of high flexibility, energy autonomy, and high conformability emerges as a promising active self-powered sensing for physiological signal monitoring, including respiratory activities.

Here, we present a simple and low-cost strategy to achieve comfortable, lightweight, flexible, breathable, and self-powered all-nanofiber e-skin (SANES) based on TENG for real-time respiratory monitoring and diagnosis and precaution of obstructive respiratory diseases, such as obstructive sleep apnea hypopnea syndrome. The SANES is realized through a facile, and readily implementable electrospinning strategy, in which electrospun polyamides 66 (PA 66) nanofibers coated with Au electrode as the top electrification layer and polyacrylonitrile (PAN) nanofibers coated with Au electrode as the bottom electrification layer, which has the advantages of high sensitivity (0.217 kPa^{-1}), good flexibility, wearing comfort, and convenience. The numerous spatial micro-to-nano-hierarchical porous structures formed between the interlaced nanofibers provide high specific surface area for contact electrification and multiple interfibrous capillary channels for thermal-moisture transfer, endowing the SANES with good air permeability, enhanced power output, improved pressure sensitivity, and even the abilities of vibrational energy harvesting and detection. Under 3 Hz loading frequency and 10 N applied force, the SANES can achieve an open-circuit voltage of 420 V and a peak power density of $\approx 330 \text{ mW m}^{-2}$, which can light up hundreds of LEDs and charge various commercial capacitors. Moreover, a respiratory monitoring system and an obstructive sleep apnea-hypopnea diagnosing system with good stability and high accuracy and reliability are demonstrated respectively, which show great potential in wearable medical electronics and personal healthcare monitoring.

2. Results

2.1. Fabrication and Structure Design of All-Nanofiber TENG-Based E-Skin

As illustrated in **Figure 1a**, the all-nanofiber TENG-based e-skin can be attached on the abdomen to continuously monitor the real-time respiratory signals. The SANES consists of three functional layers (**Figure 1b**), i.e., top encapsulation layer, bottom substrate layer, and the middle electrification layer, in which the sandwiched PA 66 and PAN work for contact electrification pairs. One layer of Au with a thickness of 100 nm is deposited on the surface of PAN as the top electrode, while another layer of Au is deposited on the surface of PA 66 as the bottom electrode (**Figure 1c**). Afterward, PA 66 and PAN as the top and bottom covering layers are used to protect the Au electrodes from external interference, respectively. All the nanofibers are prepared by the electrospinning method and the detailed fabrication process is described in the Experimental Section. The surface morphologies of PA 66 and PAN nanofibers observed by scanning electron microscopy (SEM) are shown in **Figure 1d,e**, respectively, in which the hole structures formed by uniform nanofibers can be found. Due to the numerous 3D micro-to-nano-hierarchical pores constructed by the multilayer stacking nanofiber networks, the SANES has good breathability. The air permeability of the SANES increases with the increase of the air pressure (**Figure S1**, Supporting Information), which is comparable to that of commercial jeans ($\approx 10 \text{ mm s}^{-1}$). Considering that commercial PAN and PA 66 fibers are widely used for garments that have good biocompatibility, wearability, non-toxicity, and noninflammatory, the SANES can be used as skin contact interface. To evaluate its long-term wearing feasibility, the PAN and PA 66 nanofiber films are adhered on the volar forearm for 12 h (**Figure S2**, Supporting Information). It can be found that the PAN and PA 66 nanofiber films show almost no negative effects on the skin, such as skin stiffness, rashes, and other inflammatory reactions, which can be attributed to the excellent breathing ability of the nanofibers. A photograph of the prepared SANES with a size of $4 \times 4 \text{ cm}^2$ is exhibited in **Figure 1f**, in which the PA 66 with Au electrode deposited on the surface is exhibited at its left bottom. Similarly, the reverse side of the SANES and the PAN coated with Au can be also found in **Figure S3** in the Supporting Information. In addition, the SANES with the total thickness of $270 \mu\text{m}$ and the weight of 120 mg is rather thin, highly conformal, and easy to bend, indicating that it can be used for human friendly skin interfaced biosensors (**Figure 1g**).

The working principle of the TENG-based SANES is illustrated in **Figure 1h**, which works in a vertical contact-separation mode. The relative motion of one cycle can be simplified as a contact-separation process that occurs between the PAN and PA 66 nanofibers. Once the PAN contacts with the PA 66, electrification occurs at the interface and generates the same amount of charges with opposite polarities at the surface of the PAN and PA 66. During this process, PAN is proven to be negatively charged because of its ability to attract more electrons, while PA 66 is in the reverse case (**Figure 1h,i**). When they are separated and gradually moving away, a potential difference is established. Negative charges will be

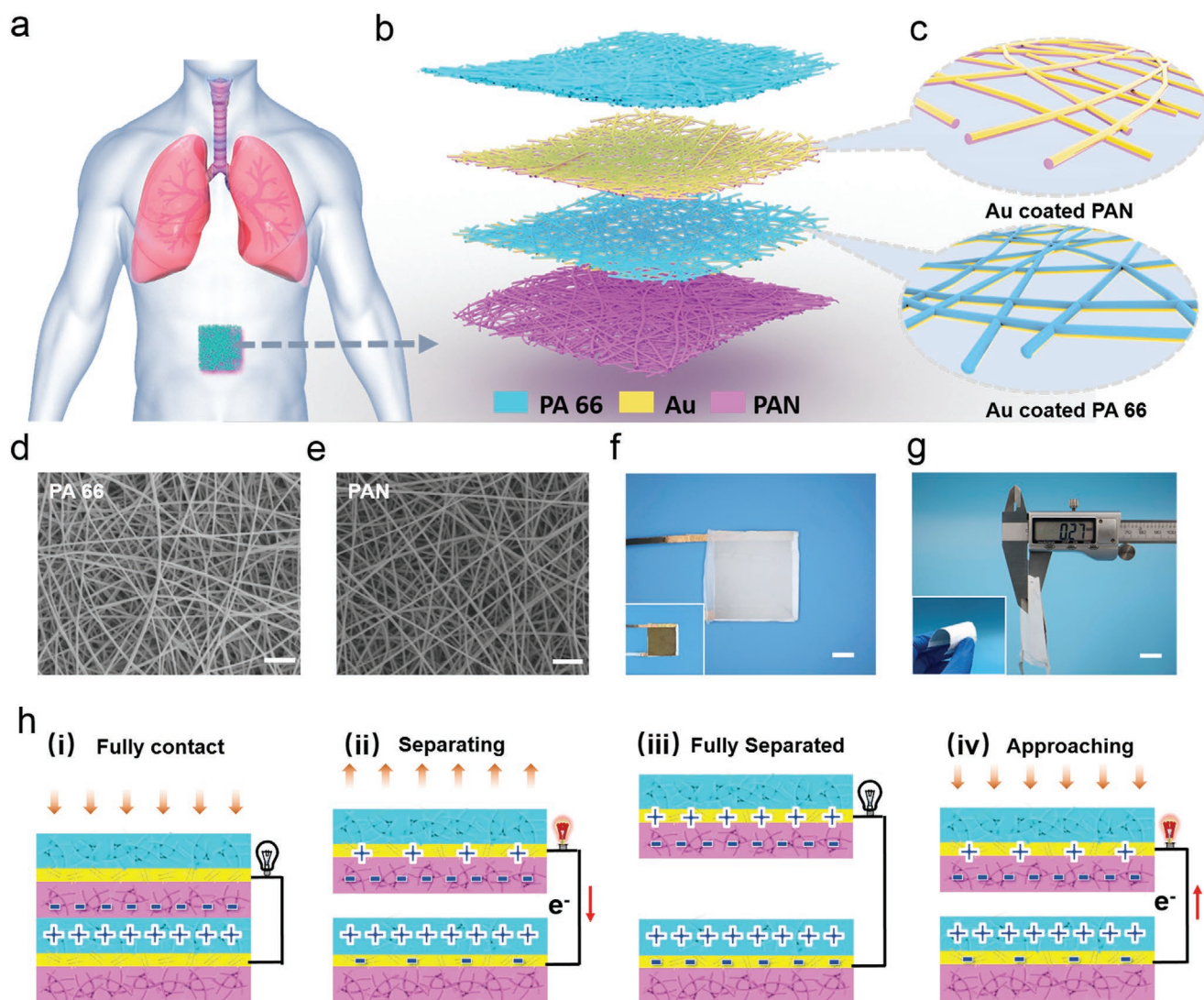


Figure 1. Structural design and working principle of the TENG-based SANES. a) Application scenario of the SANES attached on the surface of abdomen for respiratory monitoring. b) Schematic illustration of the SANES. c) Enlarged view of the layers of Au electrodes coated on the surface of PAN nanofiber film and PA 66 nanofiber film. d) Surface morphology SEM images of PA 66 (scale bar, 2 μm) and e) PAN (scale bar, 2 μm) nanofibers. f) Photographs of the SANES (scale bar, 1 cm). The inset is the photograph of the Au electrode. g) Photograph images of the SANES with a total thickness of 270 μm (scale bar, 1 cm). The inserted picture shows that it can be bent easily by fingers. h) Schematic illustration of the working mechanism of the SANES in a complete contact-separation cycle, including i) fully contact, ii) gradually separating, iii) fully separated, and iv) gradually approaching.

transferred from bottom Au electrode to top Au electrode through external circuit due to the electrostatic induction effect. The accumulated electrical potential difference between two electrodes prompts electrons to flow, generating an instantaneous electrical current (Figure 1h,ii). When the two layers are completely separated, the negative charges in the top Au layer are fully equilibrated by the electrostatic induced charges on the bottom Au electrode, reflecting the neutralization of both the positive and negative charges in this period (Figure 1h,iii). It should be noted that the accumulated charges will not be entirely annihilated. Instead, they will be maintained for a sufficiently long time due to the innate features of insulator. In the reverse case, if the upper part is approaching back to the lower part, the accumulated positive charges in top Au

electrode will flow back to bottom Au electrode through the external load to compensate for electrical potential differences (Figure 1h,iv). After the whole system returns to the initial state (Figure 1h,i), the negative charges on the top Au electrode are fully offset by the positive charges on the bottom Au electrode again. As a result, a contact-separation process between two electrodes in SANES will generate an instantaneous alternating potential and current through the external load. To obtain a more quantitative understanding of the electricity generating process, a theoretical model of the SANES is established to observe the electric potential distribution of every component under the fully separated state by a simple finite element simulation using COMSOL Multiphysics (Figure S4, Supporting Information).

2.2. Characterization of Electrical Output Performance

The electrical output performance of the SANES including open-circuit voltage (V_{OC}), short-circuit current (I_{SC}), and short-circuit charge transfer (Q_{SC}) under different loading frequencies (1–5 Hz) are quantitatively measured by a mechanical linear motor at the fixed load of 10 N (Figure S5, Supporting Information). It is found that the V_{OC} and Q_{SC} almost remain constant (420 V and 160 nC, respectively), while a gradually increasing I_{SC} (from 1.8 to 9.5 μ A) is observed as the frequencies increase from 1 to 5 Hz (Figure 2a–c). The potential reason can be attributed that V_{OC} and Q_{SC} are independent of speed, which means that the variation of movement frequency will cause no change of the V_{OC} and Q_{SC} . However, the I_{SC} depends on the relative movement speed, which presents a positive correlation feature with the increase of speed, which is further explained in

Note S1 in the Supporting Information. At the applied frequency of 3 Hz, the current density and power density of the SANES are further measured by connecting with varied external resistances (R) in series. Due to the Ohm's law, with the exponential increase of R , the current density presents a trend of initial stability and then a rapid decrease. The area power density (P) increases first and reaches its maximum to ≈ 330 mW m^{-2} at a matched resistance of ≈ 100 m Ω (Figure 2d). The P can be calculated by the equation as

$$P = \frac{I^2 R}{A} \quad (1)$$

where I is the current and A is the size area. Under normal hand patting, an SANES with a dimension of 40 \times 40 mm² (Figure S6, Supporting Information) can instantaneously light

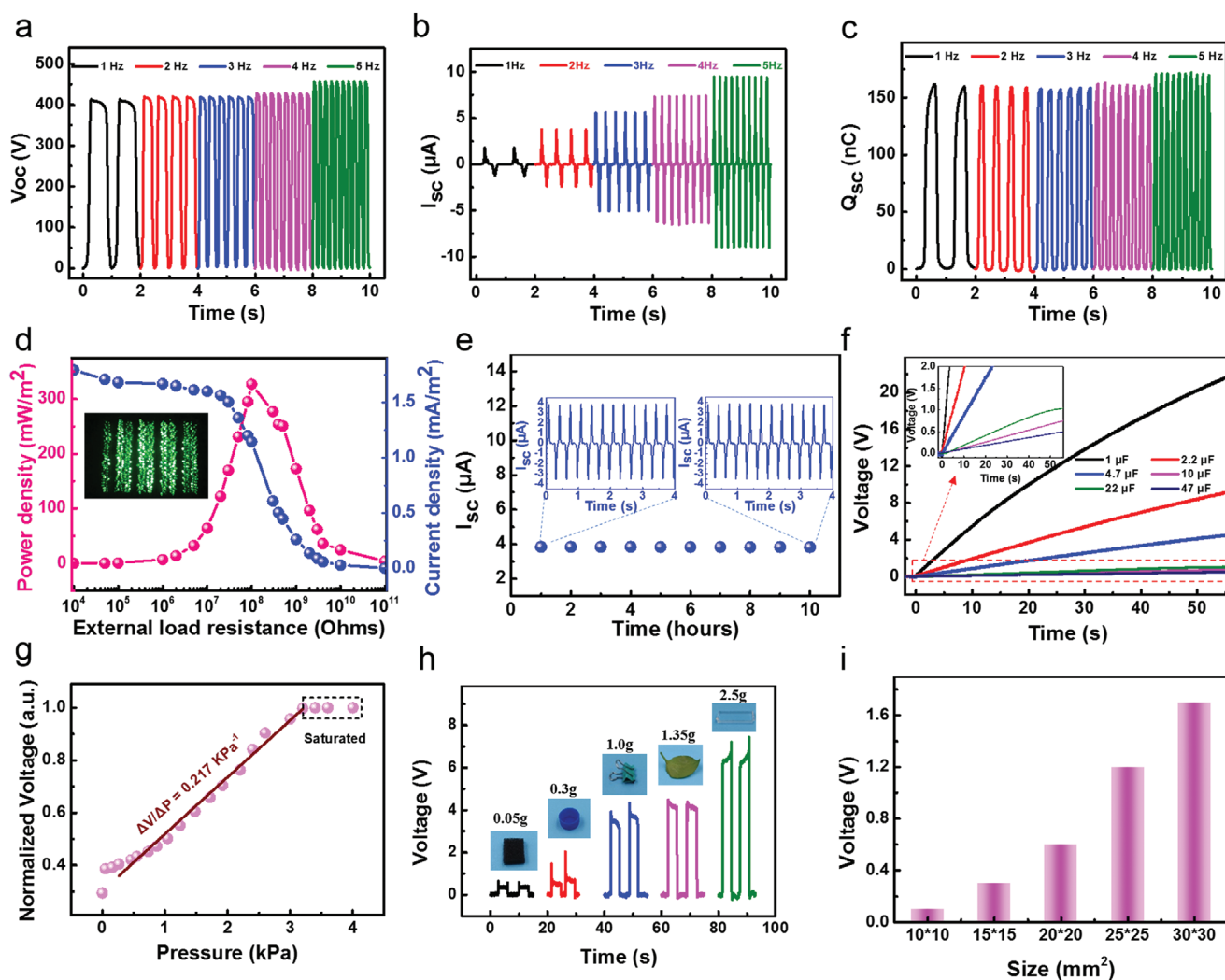


Figure 2. Electrical output performance of the SANES. a–c) Frequency-response characteristics of the SANES under different loading frequencies (1–5 Hz), including a) V_{OC} , b) I_{SC} , and c) Q_{SC} . d) Current density and peak power density under varied external resistances. The inserted photograph of lighting up over 500 LEDs by hand tapping the SANES. e) Long-term durability of the SANES for continuous contact-separation motions more than 10 h. The left and right inset figures show the corresponding output current after 1 and 10 h, respectively. f) Charging performance under different capacitors (1–47 μ F). g) Normalized output voltage response to a wide range of pressures (0–4 kPa). h) Voltage response to objects of different weights. i) Voltage response to acrylic blocks of different sizes.

up more than 500 LEDs, as inserted in Figure 2d. In addition, the long-term stability of the SANES is discussed. As shown in Figure 2e, the I_{SC} has no significant reduction after continuous loading cycles for 10 h under the pressure of 5 N and the frequency of 3 Hz, clearly demonstrating its remarkable stability and durability for long-term service. Moreover, the electricity harvested from the SANES can be further stored in energy storage devices (e.g., capacitor and battery) for later usage. The charging capabilities of the SANES to different commercial capacitors are also analyzed and compared. With the increase of capacitances of capacitors, the charging speed will become slower and the voltage value will decrease at the same time (Figure 2f). Due to its remarkable power output ability, the SANES has great application potentials in the field of wearable micro/nanopower source and self-powered sensors in the future.

The pressure sensitivity of the SANES as a function of loading force is studied, which is defined as the slope of normalized voltage versus pressure curve, i.e.,

$$S = \frac{d(\Delta V/V)}{dP} \quad (2)$$

where ΔV is the relative change in voltage, V is the saturation voltage, and P is the applied pressure. As shown in Figure 2g, the normalized voltage presents almost a linear relationship within pressure of 3 kPa, and the sensitivity is 0.217 kPa^{-1} , which is relatively high (Table S1, Supporting Information). Such good performance can be ascribed to the increase of surface roughness due to the interlacing of PAN and PA 66 nanofibers, which also facilitates the triboelectric property. Due to the excellent pressure sensitivity, the SANES is able to respond to objects with different slight weights, such as 0.05 g sponge, 0.3 g centrifugal tube cap, 1.0 g clamp, 1.35 g leaf, and 2.5 g acrylic plate. For example, it can repeatedly and steadily distinguish electrical signal differences even for the sponge with the mass of 0.05 g (Figure 2h). In addition, the SANES can distinguish the difference of electrical signals to different objects' size, which shows that the output voltages increase with the increment of area (Figure 2i). The high sensitivity of our SANES also makes it a good candidate to provide relevant information by monitoring subtle human respiration behaviors.

Due to the numerous 3D micro-to-nano-nanofiber network structure, the all-nanofiber e-skin can also effectively harvest subtle vibration energy under low frequencies. To characterize the vibrational electrical output performance of the SANES, a measuring system including a function generator, power amplifier, electrodynamic shaker, electrometer, data acquisition card, and signal acquisition system is established (Figure 3a). An electrodynamic shaker is used as an external vibration source with controlled frequency and amplitude, in which the vibration signal is generated from the function generator, then amplified via the power amplifier and finally utilized to control the vibration amplitude and frequency of the electrodynamic shaker. By adjusting the function generator and power amplifier, the SANES fixed on the shaker can generate a low-frequency sinusoidal motion, which can simulate the abdominal undulating movement of human breathing. Afterward, the output electrical signals are recorded by the electrometer and further displayed

on the terminal. By adjusting the vibration frequency and amplitude of the electrodynamic shaker, human respiration behaviors, including respiratory rate and respiratory depth, can be simulated to study its influence on electrical output. System calibration is very crucial to the measurement accuracy of the sensor in the process of use. The frequency of output signal is 0.2 Hz which is consistent with the setting frequency of shaker (Figure S7, Supporting Information), indicating our e-skin has good accuracy. Considering that the average respiratory rate of an adult ranges from 12 to 20 breaths per minute (bpm) during the rest condition,^[43] the corresponding breathing frequencies are from 0.2 to 0.33 Hz. Therefore, the V_{OC} , I_{SC} , and Q_{SC} of the SANES are measured and discussed under low frequencies (0.1–0.6 Hz). As shown in Figure 3b–d, both of the V_{OC} and Q_{SC} first increase and then reach the maximum of 5.2 V and 2.2 nC, respectively. However, the I_{SC} increases from 0.2 to 2 nA continuously. Moreover, the vibration amplitude response behaviors of SANES are also characterized. As shown in Figure 3e–g and Figure S8 in the Supporting Information, all of the electrical outputs increase with the increasing of exciting amplitude from 0.2 to 1.4 V_{pp} at a fixed vibration frequency of 0.2 Hz. The result can be explained by that the increase of amplitude will increase the applied force resulting from a larger contact-separation distance, leading to a higher electrical output. In addition, there is a good linear relationship between vibration amplitude and output voltage (Figure S9, Supporting Information). Moreover, the variation of electrical output performance at 0.33 Hz is almost consistent with that at 0.2 Hz (Figure S10, Supporting Information). Therefore, the variation of V_{OC} at different frequencies and amplitudes is able to reflect the respiratory state, such as different respiratory rates and depths. For example, respiration rate can be measured by counting the number of electrical pulses in a minute (i.e., bpm). Respiration depth is determined by the peak-to-peak amplitude. Considering that the human body may sweat in the process of practical application, it is necessary to investigate the effect of relative humidity (RH) on the electrical output. As shown in Figure S11 in the Supporting Information, although the V_{OC} decrease gradually with the increase of RH from 30% to 85%, there is still a certain electrical output even at 85% RH, indicating that our e-skin can work well in high humidity.^[44]

2.3. Respiratory Monitoring

It is well known that respiratory characteristics including respiratory rate and depth are the primary vital signs to help assess the physical and mental state of a person, which are important indexes in the early recognition of related diverse illnesses.^[45,46] The as-fabricated flexible, breathable, and self-powered SANES aims to provide smart wearable sensors that is capable of monitoring human respiratory signals for disease prevention and medical diagnosis in a rapid, real-time, noninvasive, and user-interactive way. Here, by attaching an SANES on a personal abdomen, the undulatory respiration motion can be detected through the real-time electrical signals (Figure S12, Supporting Information), the detailed procedure is described in the Experimental Section. In order to avoid the influence of chest interference and external environment, it is essential to optimize signal

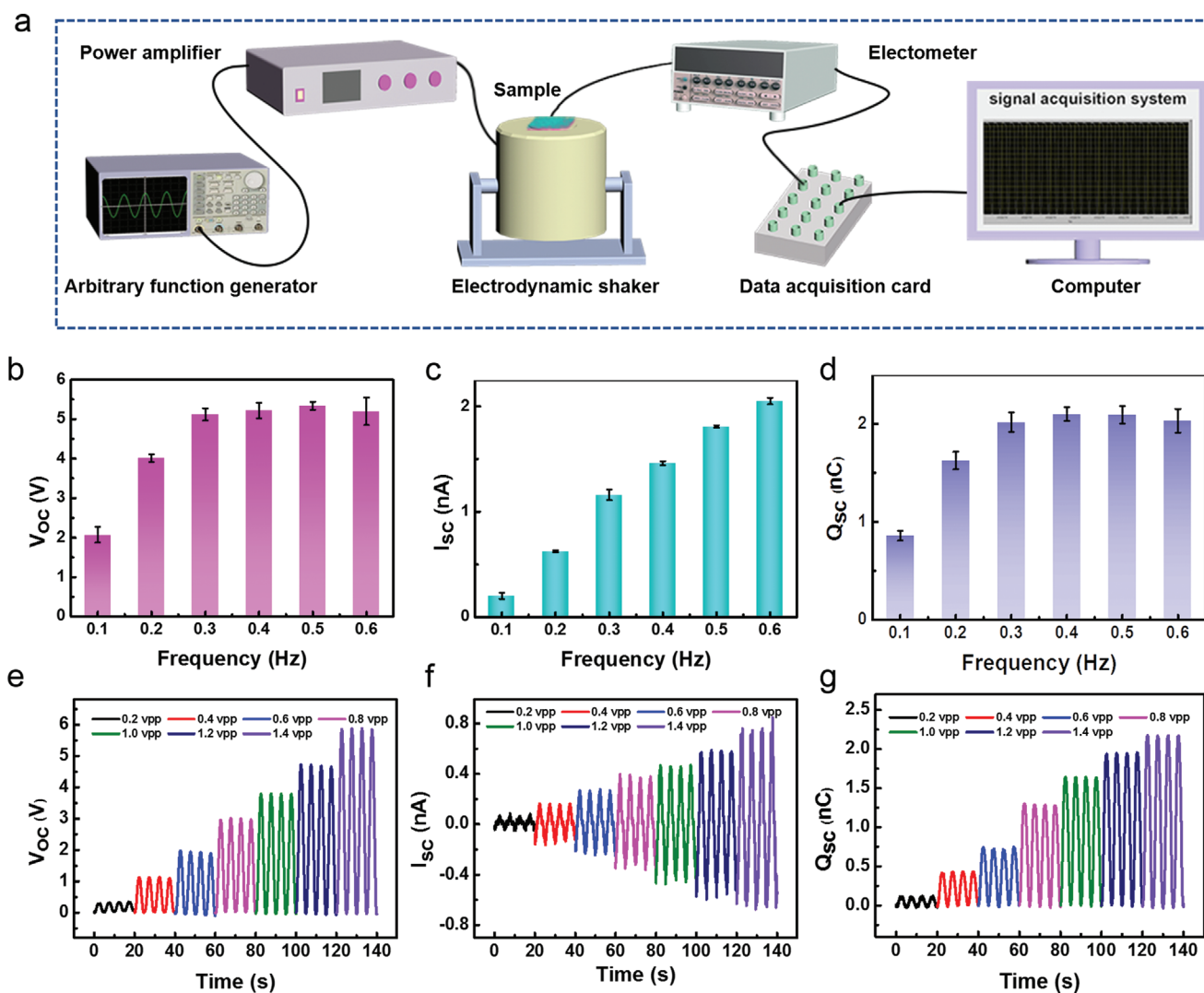


Figure 3. Vibrational electrical signal output for simulating human respiration. a) Schematic illustration of the experimental setup for vibration test. b) V_{OC} , c) I_{SC} , and d) Q_{SC} of the SANES under different exciting frequencies (0.1–0.6 Hz) at the amplitude of 1.0 V_{pp} . e) V_{OC} , f) I_{SC} , and g) Q_{SC} of the SANES under varied vibration amplitudes (0.2–1.4 V_{pp}) at the frequency of 0.2 Hz.

processing specially designed for detecting respiratory patterns. Under normal circumstances, the average respiratory rate of an adult ranges from 12 to 20 bpm, and the corresponding breathing frequency is between 0.2 and 0.33 Hz. Therefore, digital signal processing method is employed to process the original respiratory data, especially in the low frequency range. Detailed procedures of data processing in this work are demonstrated in Figure 4a. A SANES with $4 \times 4 \text{ cm}^2$ is attached above the navel of the volunteer's abdomen by a medical bandage. Original respiratory signal from the SANES is collected using an analogue-to-digital conversion (ADC), followed by conditioning and signal processing with a finite impulse response low-pass filter which is designed in LabVIEW. After data processing, the signals are smooth and the false pulses are greatly reduced. In addition, the high-frequency portion of the signal is also attenuated. Finally, the processed signals, including respiratory rate, respiratory interval, and respiratory intensity can be obtained. The detailed calculation method is shown in Note S2

in the Supporting Information. Figure 4b shows a volunteer breathing in a normal and quiet sitting state, from which the corresponding respiratory rate, respiratory interval time, and respiratory intensity are 18 bpm, 3.34 s and nearly 0.4, respectively (Figure 4c). It is worth noting that the rhythm of breathing is regular and the amplitude is even, which are in accordance with the normal respiratory activities of an adult at rest state. A real-time recording of individual different respiratory patterns, including breath holding, shallow, normal, deep, and fast, are shown in Figure 4d, indicating that our SANES can accurately distinguish different breathing states. In addition, there are significant differences in respiratory rate and respiratory intensity under different breathing states. For example, the respiratory rate is 56 bpm for fast breathing state, while for slow breathing state, the respiratory rate is 15 bpm. The respiratory intensity of shallow breathing, normal breathing, and deep breathing are approximate 0.2, 0.5, and 0.9, respectively. The corresponding respiratory monitoring video of SANES is

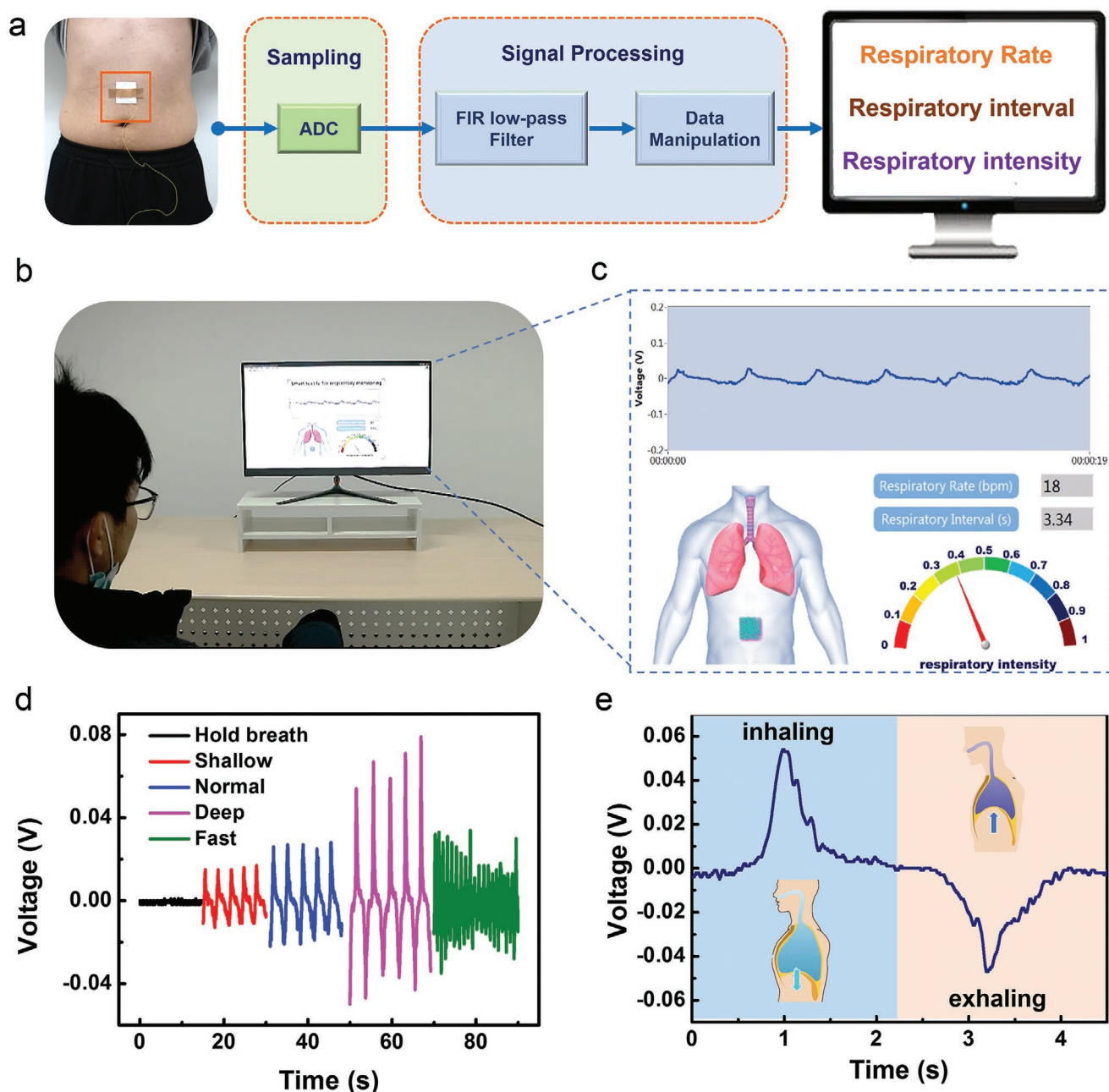


Figure 4. Respiratory monitoring system. a) Flowchart of data acquisition and processing for respiratory monitoring. Photograph showing that an SANES is attached on the abdomen by a medical bandage. b) Photograph of the respiratory signal monitoring state. c) The enlarged view of interface of the real-time respiratory monitoring system, including respiratory electrical signal, respiratory rate, respiratory interval, and respiratory intensity. d) Real-time voltage signals of different respiratory states, including breath holding, shallow, normal, deep, and fast. e) One complete respiratory waveform containing process of inhaling and exhaling.

demonstrated in Movie S1 in the Supporting Information. In particular, one complete breathing cycle involves the inhalation and exhalation process. On inhalation, the diaphragm muscle contracts and pulls downward to increase the volume of the abdomen, which in turn contacts the SANES to generate a positive V_{OC} signal. In reverse, on exhalation, the diaphragm muscle expands and pulls upward to decrease the volume of the abdomen, which releases the SANES to generate a V_{OC} signal in an opposite direction (Figure 4e). Therefore, our SANES has

a good accuracy and stability, which is available for respiratory monitoring.

2.4. Obstructive Sleep Apnea-Hypopnea Syndrome Diagnosing

Thanks to the capability of detecting respiratory signals with high accuracy and reliability, the SANES can be further developed to diagnose the severity of OSAHS and provide

precaution for associated complications. OSAHS is considered the most common organic sleep disorder by the World Health Organization, with an estimated prevalence of 9% to 38% in the population.^[47] Moreover, it is estimated that nearly 80% patients of OSAHS are still undiagnosed and untreated, which may increase risk of severe health problems, such as Alzheimer's disease, insulin resistance, strokes, hypertension, and coronary disease. The commonly used diagnostic method for sleep-related breathing disorders is polysomnography, which is a multimode recording of sleep behavior based on the participation of laboratory and technical personnel. However, it is cumbersome for patients, labor intensive, and difficult to access in many laboratories.^[48,49]

As illustrated in **Figure 5a**, the OSAHS is a breathing disorder characterized by repetitive episodes of airflow reduction or cessation during sleep due to pharyngeal narrowing, resulting in acute gas exchange abnormalities and sleep fragmentation. An obstructive apnea is defined as a complete cessation of airflow for at least 10 s. Similarly, a 30–50% reduction respiratory

amplitude in thoracoabdominal movement for at least 10 s is considered as hypopnea.^[50,51] Here, a diagnosing system for OSAHS is shown in **Figure 5b**, which includes a volunteer with an SANES on his abdomen, an acquisition module, and a real-time data analysis and interface output platform. In order to measure the respiratory signal characteristics of OSAHS symptoms, the volunteer controls deliberately his breath to simulate the hypoventilation and cessation of breathing. After a period of measurement, the electrical signal characteristics of three typical respiratory states are presented in **Figure 5c–e**. As shown in **Figure 5c**, the electrical signal is regular, in which the average interval and amplitude under normal breathing state are 2.5 s and 0.035 V, respectively. While a significant reduction of amplitude for 12 s and apnea time for 15 s are observed in **Figure 5d,e**, respectively, indicating that obstructive respiratory events occur. In addition, the amplitudes of electrical signals reduce to 42% and 98% in the hypopnea state and apnea state, respectively. The corresponding real-time OSAHS monitoring process is demonstrated in **Movie S2** in the Supporting

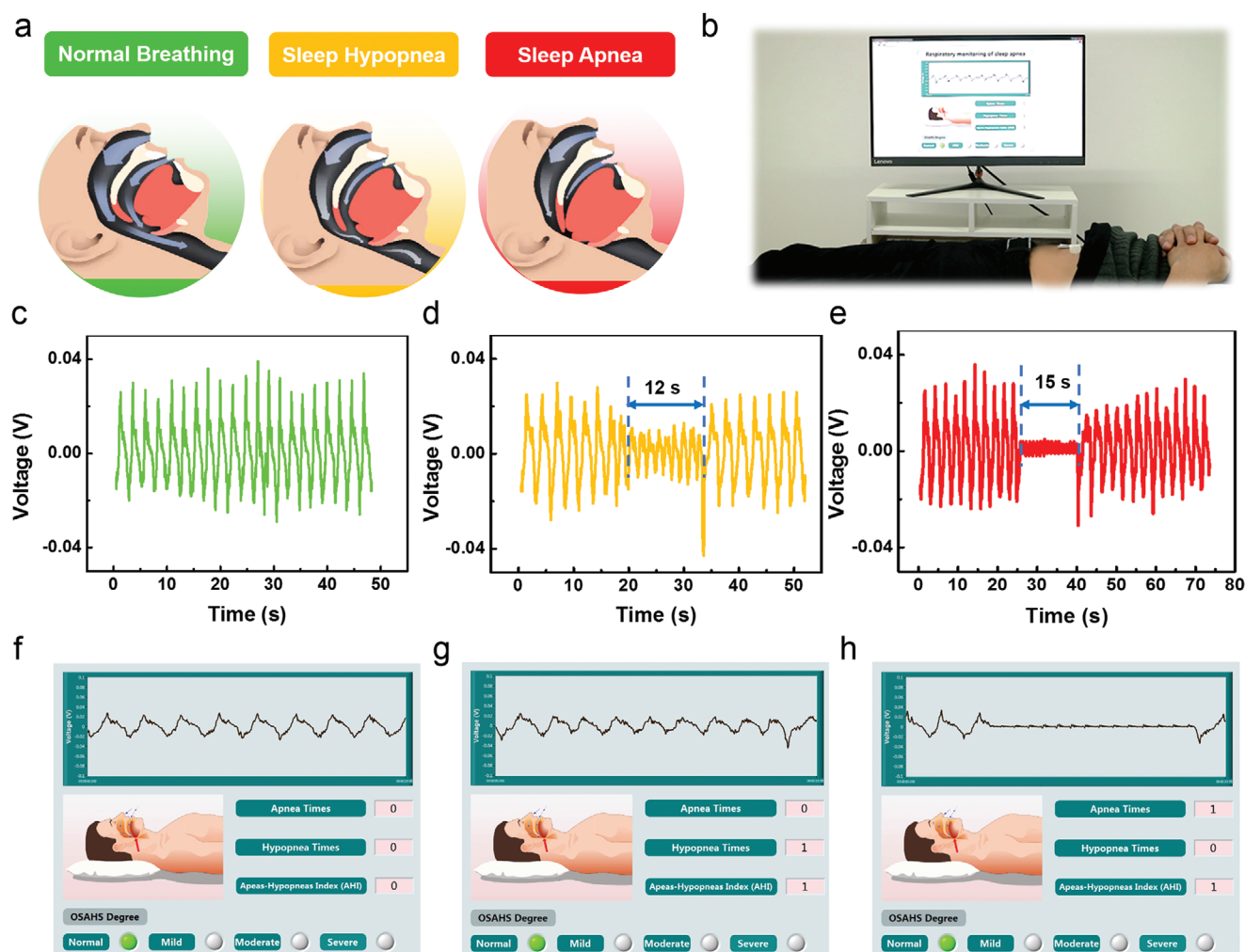


Figure 5. Obstructive sleep apnea-hypopnea syndrome diagnosis system. a) The respiratory airway states while asleep. The left, middle, and right images are normal, narrowed, and closed airways, respectively. b) The photograph showing that the SANES is used for obstructive sleep apnea-hypopnea syndrome diagnosing. c–e) Real-time voltage signals under different sleep respiratory states, including c) normal, d) hypopnea, and e) apnea. f–h) The sleep respiratory state judgment based on the voltage signals.

Information. To assess the severity of OSAHS, further analysis of the real-time respiratory signals is necessary. The number of the OSAHS symptom can be counted and then displayed, as exhibited in Figure 5f–h. The apnea-hypopnea index (AHI) is an index to evaluate the degree of OSAHS, which is defined as the total number of apneas and hypopneas per hour of sleep. The relationship between the AHI and the severity criteria for OSAHS in Table S2 in the Supporting Information shows that the sleep-related obstructive breathing events can be rated as mild (5–15 events h^{-1} of sleep), moderate (15–30 events h^{-1} of sleep), or severe (greater than 30 events h^{-1} of sleep). According to the severity level, the alert button can turn gray into green, yellow, orange, and red depending on the severity from normal to severe. For example, when the AHI is 6, the button turns on yellow after a specified period of time (Movie S3, Supporting Information), indicating that the severity of OSAHS is mild. Therefore, our SANES provides a simple and noninvasive detection method, which is not only conducive to monitoring OSAHS and preventing other complications but also helps to improve sleep quality and human respiratory health.

3. Conclusions

In summary, we have successfully developed a breathable, flexible, comfortable, and self-powered TENG-based e-skin with high sensitivity and excellent stability through a readily implementable electrospinning method for real-time respiratory signals monitoring and obstructive sleep apnea-hypopnea syndrome diagnosing. Taking the advantage of the 3D micro-to-nanoporous hierarchical structure of nanofiber films, the SANES can not only achieve a remarkable maximum areal power density of 330 mW m^{-2} but also respond to tiny vibration energy with a high sensitivity of 0.217 kPa^{-1} . In addition, a real-time respiratory monitoring system with high accuracy and stability has been designed to record respiratory information, including respiratory rate, respiratory interval, and respiratory intensity. Moreover, an OSAHS diagnosing system has been developed for detection of apnea and hypopnea during sleep and severity assessment of OSAHS. We envision that our work can provide a promising strategy for personal respiratory health monitoring, auxiliary medical diagnosis of sleep disorders, and smart wearable medical electronics.

4. Experimental Section

Fabrication of All-Nanofiber E-Skin: 1) PAN ($M_w = 150\,000$, Aladdin Chemical Co. Ltd) powder was dissolved in *N,N*-dimethylformamide at concentration of 10 wt% and then placed in the plastic syringe equipped with a 20-gauge metal needle with an injection rate of 0.5 mL h^{-1} . A high voltage of 20 kV was applied between the needle and collectors (aluminum foil or PA 66 nanofibers sputtered with Au film) at a distance of 15 cm. After electrospinning, nanomembranes were dried overnight under vacuum at room temperature to remove the residual solvent for later use. 2) 20 wt% PA 66 ($M_w = 18\,000$, Aladdin Chemical Co. Ltd) powder was dissolved in the mixed solution of formic acid and acetic acid with the volume ratio of 1:1 using a magnetic stirrer for 4 h. PA 66 solution was fed into a plastic syringe fitted with a 20-gauge stainless steel blunt needle. The injection rate was adjusted to 0.5 mL h^{-1} . A stable DC voltage of 25 kV was used to provide the power for the formation of

continuous jets, resulting in the deposition of nanofibers on the grounded stainless plate covered with different substrates, including aluminum foil or PAN nanofibers sputtered with Au film. The electrospinning distance between the needle tip and the collector was set as 15 cm. The nanofilms were dried overnight under vacuum at room temperature. 3) A gold layer with a nominal thickness of 100 nm was formed on the surface of the PAN and PA66 nanofiber films by using the physical vapor deposition method (PVD, PVD75 Kurt J. Lesker). During the deposition process, power supply was set to 100 W, chamber pressure for argon was set to 6 mTorr, and the deposition time was 10 min.

Implementation Process of the E-Skin: First, the human skin was wiped with alcohol and then the e-skin was fixed 50 mm above the abdominal navel by medical tape. The lead out electrodes of the e-skin were connected with data acquisition card followed by signal processing with Labview program on the computer.

Characterizations and Measurements: The pressure-dependent air permeability was measured by using an air permeability apparatus (TQD-G1, Jinan Labthink Instrument Co. Ltd., China) according to the American Society For Testing and Materials D 737 standard test method. The surface morphology of nanofibers was characterized by field emission scanning electron microscope (Hitachi SU8020). A programmable electrometer (Keithley, model 6514) was used to test the open-circuit voltage, short-circuit current, and transferred charges. The periodic contact and separation movements were applied by a commercial linear mechanical motor (LinMot, E1100). The applied force on the e-skin was measured by a compression dynamometer (Vernier LabQuest Mini). For vibration test, function generator (AFG3102C, TEKTRONIX), power amplifier (LA-800 Power Amplifier, YMC), and electrodynamic shaker (JCK-10) were applied. The software platform was constructed on the basis of LabVIEW.

Supporting Information

Supporting Information is available from the Wiley Online Library or from the author.

Acknowledgements

X.P. and K.D. contributed equally to this work. The authors are grateful for the supports received from Minister of Science and Technology (Grant Nos. 2016YFA0202701 and 2016YFA0202703), the Beijing Municipal Natural Science Foundation (Grant No. 2212052), and the University of Chinese Academy of Sciences. No formal approval for the experiments involving human volunteers was required. The volunteers took part following informed consent.

Conflict of Interest

The authors declare no conflict of interest.

Data Availability Statement

The data that support the findings of this study are available from the corresponding author upon reasonable request.

Keywords

electronic skins, electrospun nanofibers, respiratory monitoring, sleep-disordered breathing diagnosis, triboelectric nanogenerators

Received: April 14, 2021
Revised: May 10, 2021
Published online:

- [1] Y. Xin, T. Liu, Y. Xu, J. Zhu, T. Lin, X. Zhou, *Sens. Actuators, A* **2019**, 296, 357.
- [2] O. Thiabgoh, T. Eggers, M.-H. Phan, *Sens. Actuators, A* **2017**, 265, 120.
- [3] T. Dinh, T. Nguyen, H. P. Phan, N. T. Nguyen, D. V. Dao, J. Bell, *Biosens. Bioelectron.* **2020**, 166, 112460.
- [4] T. Mauri, C. Turrini, N. Eronia, G. Grasselli, C. A. Volta, G. Bellani, A. Pesenti, *Am. J. Respir. Crit. Care Med.* **2017**, 195, 1207.
- [5] O. Roca, G. Hernandez, S. Diaz-Lobato, J. M. Carratala, R. M. Gutierrez, J. R. Masclans, *Crit. Care* **2016**, 20, 109.
- [6] P. Jagadev, L. I. Giri, *Infrared Phys. Technol.* **2020**, 104, 103117.
- [7] Y. Liu, L. Zhao, R. Avila, C. Yiu, T. Wong, Y. Chan, K. Yao, D. Li, Y. Zhang, W. Li, Z. Xie, X. Yu, *Mater. Today Phys.* **2020**, 13, 100199.
- [8] H. Fang, J. Lin, Z. Hu, H. Liu, Z. Tang, T. Shi, G. Liao, *Sens. Actuators, B* **2020**, 304, 127313.
- [9] Y. Luo, Y. Pei, X. Feng, H. Zhang, B. Lu, L. Wang, *Mater. Lett.* **2020**, 260, 126945.
- [10] Y. Pang, J. Jian, T. Tu, Z. Yang, J. Ling, Y. Li, X. Wang, Y. Qiao, H. Tian, Y. Yang, T. L. Ren, *Biosens. Bioelectron.* **2018**, 116, 123.
- [11] D. Wang, D. Zhang, P. Li, Z. Yang, Q. Mi, L. Yu, *Nano-Micro Lett.* **2021**, 13, 57.
- [12] H. Wang, S. Li, Y. Wang, H. Wang, X. Shen, M. Zhang, H. Lu, M. He, Y. Zhang, *Adv. Mater.* **2020**, 32, 1908214.
- [13] M. Wang, J. Zhang, Y. Tang, J. Li, B. Zhang, E. Liang, Y. Mao, X. Wang, *ACS Nano* **2018**, 12, 6156.
- [14] B. Zhang, Y. Tang, R. Dai, H. Wang, X. Sun, C. Qin, Z. Pan, E. Liang, Y. Mao, *Nano Energy* **2019**, 64, 103953.
- [15] Y.-Y. Chiu, W.-Y. Lin, H.-Y. Wang, S.-B. Huang, M.-H. Wu, *Sens. Actuators, A* **2013**, 189, 328.
- [16] Z. Liu, Z. Zhao, X. Zeng, X. Fu, Y. Hu, *Nano Energy* **2019**, 59, 295.
- [17] Z. Zhao, C. Yan, Z. Liu, X. Fu, L. M. Peng, Y. Hu, Z. Zheng, *Adv. Mater.* **2016**, 28, 10267.
- [18] J. Park, S. Park, S. Ahn, Y. Cho, J.-J. Park, H. Shin, *IEEE Sens. J.* **2020**, 20, 12628.
- [19] D. Wang, D. Zhang, Y. Yang, Q. Mi, J. Zhang, L. Yu, *ACS Nano* **2021**, 15, 2911.
- [20] D. Zhang, Z. Xu, Z. Yang, X. Song, *Nano Energy* **2020**, 67, 104251.
- [21] F. Yi, L. Lin, S. Niu, P. K. Yang, Z. Wang, J. Chen, Y. Zhou, Y. Zi, J. Wang, Q. Liao, Y. Zhang, Z. L. Wang, *Adv. Funct. Mater.* **2015**, 25, 3688.
- [22] H. Zhang, J. Zhang, Z. Hu, L. Quan, L. Shi, J. Chen, W. Xuan, Z. Zhang, S. Dong, J. Luo, *Nano Energy* **2019**, 59, 75.
- [23] Z. Zhang, J. Zhang, H. Zhang, H. Wang, Z. Hu, W. Xuan, S. Dong, J. Luo, *Nanoscale Res. Lett.* **2019**, 14, 354.
- [24] M. L. Hammock, A. Chortos, B. C. Tee, J. B. Tok, Z. Bao, *Adv. Mater.* **2013**, 25, 5997.
- [25] X. Peng, K. Dong, C. Ye, Y. Jiang, S. Zhai, R. Cheng, D. Liu, X. Gao, J. Wang, Z. L. Wang, *Sci. Adv.* **2020**, 6, eaba9624..
- [26] U. Khan, T. H. Kim, H. Ryu, W. Seung, S. W. Kim, *Adv. Mater.* **2017**, 29, 1603544.
- [27] R. Dahiya, *P. IEEE* **2019**, 107, 247.
- [28] K. Dong, Z. Wu, J. Deng, A. C. Wang, H. Zou, C. Chen, D. Hu, B. Gu, B. Sun, Z. L. Wang, *Adv. Mater.* **2018**, 30, 1804944.
- [29] Y. Jiang, K. Dong, X. Li, J. An, D. Wu, X. Peng, J. Yi, C. Ning, R. Cheng, P. Yu, Z. L. Wang, *Adv. Funct. Mater.* **2020**, 31, 2005584.
- [30] X. Wang, L. Dong, H. Zhang, R. Yu, C. Pan, Z. L. Wang, *Adv. Sci.* **2015**, 2, 1500169.
- [31] J. C. Yang, J. Mun, S. Y. Kwon, S. Park, Z. Bao, S. Park, *Adv. Mater.* **2019**, 31, 1904765.
- [32] A. Chortos, J. Liu, Z. Bao, *Nat. Mater.* **2016**, 15, 937.
- [33] Z. L. Wang, *Nano Energy* **2020**, 68, 104272.
- [34] Z. L. Wang, *Adv. Energy Mater.* **2020**, 10, 2000137.
- [35] Z. L. Wang, *Faraday Discuss.* **2015**, 176, 447.
- [36] K. Dong, X. Peng, J. An, A. C. Wang, J. Luo, B. Sun, J. Wang, Z. L. Wang, *Nat. Commun.* **2020**, 11, 1.
- [37] K. Dong, J. Deng, W. Ding, A. C. Wang, P. Wang, C. Cheng, Y. C. Wang, L. Jin, B. Gu, B. Sun, Z. L. Wang, *Adv. Energy Mater.* **2018**, 8, 1801114.
- [38] Z. Wu, T. Cheng, Z. L. Wang, *Sensor* **2020**, 20, 2925.
- [39] J. Wang, S. Li, F. Yi, Y. Zi, J. Lin, X. Wang, Y. Xu, Z. L. Wang, *Nat. Commun.* **2016**, 7, 12744.
- [40] J. Wang, C. Wu, Y. Dai, Z. Zhao, A. Wang, T. Zhang, Z. L. Wang, *Nat. Commun.* **2017**, 8, 88.
- [41] K. Dong, X. Peng, Z. L. Wang, *Adv. Mater.* **2019**, 32, 1902549.
- [42] Z. Wu, W. Ding, Y. Dai, K. Dong, C. Wu, L. Zhang, Z. Lin, J. Cheng, Z. L. Wang, *ACS Nano* **2018**, 12, 5726.
- [43] P. B. Lovett, J. M. Buchwald, K. Stürmann, P. Bijur, *Annu. Emerg. Med.* **2005**, 45, 68.
- [44] J. Jiang, J.-E. Lee, K.-S. Kim, K. Suganuma, *J. Alloys Compd.* **2008**, 462, 244.
- [45] M. A. Cretikos, R. Bellomo, K. Hillman, J. Chen, S. Finfer, A. Flabouris, *Med. J. Aust.* **2008**, 188, 657.
- [46] S. Fleming, M. Thompson, R. Stevens, C. Heneghan, A. Plüddemann, I. Maconochie, L. Tarassenko, D. Mant, *Lancet* **2011**, 377, 1011.
- [47] J. E. Hernandez, E. Cretu, *Biomed. Signal Process. Control* **2020**, 61, 102023.
- [48] R. Farre, J. M. Montserrat, D. Navajas, *Eur. Respir. J.* **2004**, 24, 1052.
- [49] E. J. Olson, W. R. Moore, T. I. Morgenthaler, P. C. Gay, B. A. Staats, *Mayo Clin. Proc.* **2003**, 78, 1545.
- [50] R. L. Riha, *J. Thorac. Dis.* **2015**, 7, 1373.
- [51] R. B. Berry, R. Brooks, C. E. Gamaldo, S. M. Harding, C. Marcus, B. V. Vaughn, *Rules, Terminology and Technical Specifications*, Vol. 176, American Academy of Sleep Medicine, Darien, IL **2012**, p. 2012.